Real-Time Worldwide Monitoring of Ionospheric Scintillation Using Geodetic Detrending

Yu Yin, Guillermo González-Casado, José Miguel Juan, Cristhian C. Timote, Jorge García-Mateos, Raul Orús-Pérez, Angela Aragon-Angel, and Adria Rovira-Garcia, *Senior Member, IEEE*

***Abstract*— A real-time (RT) ionospheric scintillation monitoring tool has been developed based on the observations from geodetic receivers in Global Navigation Satellite System (GNSS) networks. It extends the application of the geodetic detrending (GD) technique to make it work with RT products for satellite orbit, tropospheric, and satellite/receiver clock corrections applied to uncombined GNSS signals. It overcomes the limitation of the coverage of specialized ionospheric scintillation monitoring receivers (ISMRs), enabling worldwide monitoring. Through this novel tool, it is possible to supply large RT information about scintillation activity to both GNSS users and the scientific community. The performance of the tool has been validated by cross checking with postprocessing (PP) GD results and reference data from a collocated ISMR in a period with intense scintillation activity. The results demonstrate high consistency for the phase scintillation index between the RT tool based on geodetic receivers operating at 1 Hz and the reference ISMR. The few outliers detected are related with the different processing, location, and sampling frequency from each type of receiver.**

***Index Terms*— Geodetic detrending (GD), Global Navigation Satellite System (GNSS), ionospheric scintillation, real time (RT), worldwide monitoring.**

I. Introduction

IONOSPHERIC scintillation refers to the effects produced in trans-ionospheric radio signals by rapid fluctuations in the ionospheric electron density. Scintillation poses a significant threat to Global Navigation Satellite System (GNSS) applications, which rely on L-band radio signals [1], [2]. Scintillation activity is frequent and severe in both high- and low-latitude regions, producing signal amplitude fading, fast fluctuations, and even cycle slips (CSs) on the carrier phase [1], [3], [4]. The effects of scintillation on GNSS signals are typically measured by two indexes denoted as S_4 and σ_ϕ, which characterize signal intensity fading and carrier phase fluctuations, respectively [4], [5], [6]. Those indexes are produced by specialized receivers known as ionospheric scintillation monitoring receivers (ISMRs). Currently, they are deployed in some regional networks, such as Canadian High Arctic Ionospheric Network (CHAIN), Space Weather Service in Australia, Brazilian network with the ISMR Query Tool, or Italian electronic space weather upper atmosphere [6], [7], [8], [9]. However, there are a large number of regions that are not presently covered by the existing ISMR networks. Additionally, not all ISMR networks offer real-time (RT) or RINEX data availability to users, which limits their use in time-sensitive applications.

Geodetic receivers providing high-rate data are available worldwide, providing an alternative to the ISMRs. Several agencies offer free access to hundreds of stations equipped with geodetic-grade receivers, supplying a large quantity of data on a global or regional scale. For example, the International GNSS Service (IGS) has more than 300 ground stations worldwide distributed equipped with receivers offering RT GNSS carrier phase measurements at 1-Hz sampling frequency.

However, due to unstable clocks in geodetic receivers, detrending techniques are necessary to filter out high-frequency fluctuations unrelated with scintillation. The geodetic detrending (GD) technique has been developed and demonstrated in a series of previous studies [10], [11], [13], allowing accurate ionospheric scintillation monitoring. Since scintillation mainly involves high-frequency fluctuations, the GD technique requires geodetic receivers to provide high-rate data at 1 Hz. With the assistance of the GD technique, a σ_ϕ index is computed over 60 s from L1 carrier phases sampled at 1 Hz. Our previous studies show that, for scintillation events lasting more than a few seconds, GD-derived indexes are fully consistent with those from ISMRs using measurements sampled with frequencies of 50 Hz or larger [10], [11], [12], [13], offering a cost-effective solution for global scintillation monitoring using the existing geodetic receiver networks.

The present study aims to validate the feasibility of applying the GD technique to RT observations, using RT products for geodetic corrections and to demonstrate the potential for extending its use to RT applications based on data transmitted by the IGS RT Service. With the upcoming solar maximum of the 25th solar cycle, this approach will improve RT

Received 21 October 2024; revised 20 December 2024; accepted 6 January 2025. Date of publication 10 January 2025; date of current version 27 January 2025. This work was supported in part by MCIN/AEI/10.13039/501100011033/FEDER, UE under Project PID2022-138485OB-I00 and Project CNS2022-135383; and in part by European Space Agency under Contract RT-WMIS 4000137762/22/NL/GLC/ov. The work of Yu Yin was supported by China Scholarship Council under Grant 202006020025. *(Corresponding author: Yu Yin.)*

Yu Yin, José Miguel Juan, Cristhian C. Timote, Jorge García-Mateos, Angela Aragon-Angel, and Adria Rovira-Garcia are with the Research Group of Astronomy and Geomatics (gAGE), Universitat Politècnica de Catalunya (UPC), 08034 Barcelona, Spain (e-mail: yu.yin@upc.edu).

Guillermo González-Casado is with the Research Group of Astronomy and Geomatics (gAGE), Universitat Politècnica de Catalunya (UPC), 08034 Barcelona, Spain, and also with the Institut d'Estudis Espacials de Catalunya (IEEC), 08860 Castelldefels, Spain.

Raul Orús-Pérez is with European Space Agency (ESA), 2201 AZ Noordwijk, The Netherlands.

Digital Object Identifier 10.1109/LGRS.2025.3528179

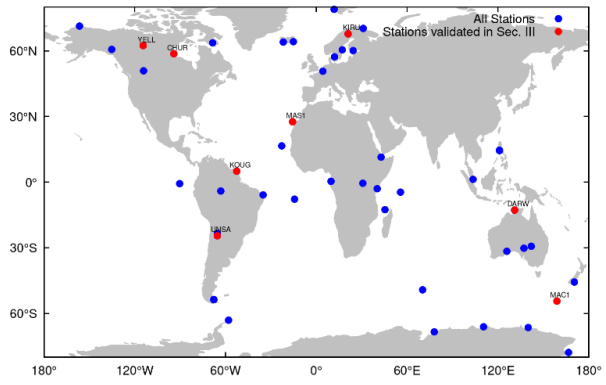

Fig. 1. RT GONet, currently consisting of 47 stations (blue and red dots). Stations in red have been used for the validation study presented in Section III.

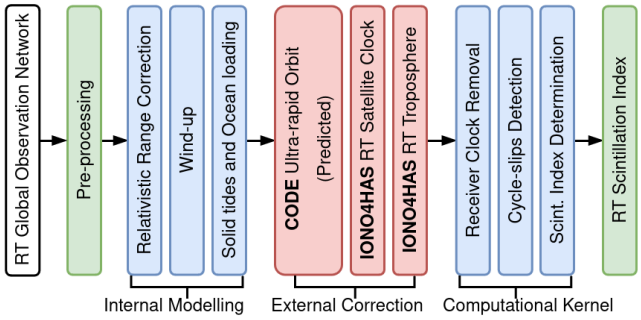

Fig. 2. Processing workflow of the RT tool implemented: from the RT GONet of geodetic GNSS receivers managed by the tool to the delivery of the RT scintillation index.

scintillation monitoring, which is crucial to prevent GNSS users from this phenomenon.

II. Real-Time GD

The RT GD implementation utilizes GNSS observations at a sampling frequency of 1 Hz collected by the Bundesamt für Kartographie und Geodäsie NTRIP Client software [14] via broadcasters from IGS, AUSCORS, EUREF, IGN, and RBMC networks. The tool began operation and testing on the day of year (DoY) 104, 2023, with an initial set of eight stations strategically located in high- and low-latitude regions (red dots in Fig. 1), where ionospheric activity is of interest. A validation study for these stations is presented in Section III. At present, this group of stations is a subset of the total set of 47 receivers (including three collocated pairs), hereafter referred to as the Global Observation Network (GONet), which are being processed by the RT tool, and their locations are shown in Fig. 1.

The workflow of the RT tool is outlined in Fig. 2. Preprocessed measurements from individual receivers in the GONet go through three calculation modules.

1) *Internal Modeling:* It handles relativistic, wind-up, and Earth deformation effects, which are accurately modeled using known equations [17].
2) *External Correction:* Corrections for satellite orbit, clock, and tropospheric delay are applied from external sources. It is crucial that such external products are available in RT. Specifically, orbits are derived from the predicted part of the ultrarapid products computed by the Center for Orbit Determination in Europe (CODE), updated every 2 h. Clock corrections (updated every 30 s) and troposphere corrections (updated every 300 s) are obtained from the Fast-PPP Central Processing Facility [15] under the IONO4HAS activity [16].
3) *Computational Kernel:* This is where the core GD algorithm is executed, removing the receiver clock offsets, detecting CSs, and finally calculating the scintillation index σ_ϕ [10], [12].

All these processes have been implemented for RT operation.

The RT tool is presently processing data from GPS and Galileo constellations. It calculates the 60-s σ_ϕ index from L1 signal for the stations depicted in Fig. 1. The RT scintillation products are presently accessible to the public through the link https://server.gage.upc.edu/rtwmis/. A historical database is published on the server for the receivers shown in Fig. 1, from 2nd April 2024, DoY 93, onward. Currently, the RT tool runs on a single computer, and the results have a latency of around 3 min, which includes the latency in the RT streams of measurements and the RT corrections required by the tool and the tool processing itself. Since processing can be performed separately for each receiver, it could be configured for parallel computing in different devices. Thus, latency is not expected to increase even if the number of GONet stations grows.

Sections III and IV present the validation study performed in the initial period of time, in which the RT tool began to operate, starting from DoY 104 to DoY 130 of 2023, using the 24-h period for each DoY. This approach allows us to evaluate the performance of the RT tool not only during intense scintillation events but also during the periods of low or no scintillation, ensuring that, in such periods, no false detections are produced. Due to the proximity of the time period chosen for validation to the March equinox, scintillation activity is expected in low-latitude regions. Moreover, some intense space weather events occurred in this period that enhanced scintillation at high latitudes. In particular, a coronal mass ejection in DoY 113 that triggered in DoY 114 one of the largest geomagnetic storms in the current solar cycle.

III. Accuracy Evaluation With PP GD

This section presents a straightforward comparison between the results in RT and postprocessing (PP) implementations of the GD based on the L1 carrier-phase measurements. The PP GD tool uses postprocessed products for troposphere, satellite clocks, and orbits from IGS, not available in RT, as well as RINEX archived data for the observations. It has been demonstrated and tested in previous studies [10], [11], [12], [13], showing highly stable and accurate results. The impact of using the RT products and observations instead of the postprocess ones can be assessed by means of this comparison.

Eight stations from the GONet, four high latitude and four low latitude (see Table I), have been selected to illustrate the performance of the RT tool. These stations are located in regions usually affected by moderate to intense scintillation activity.

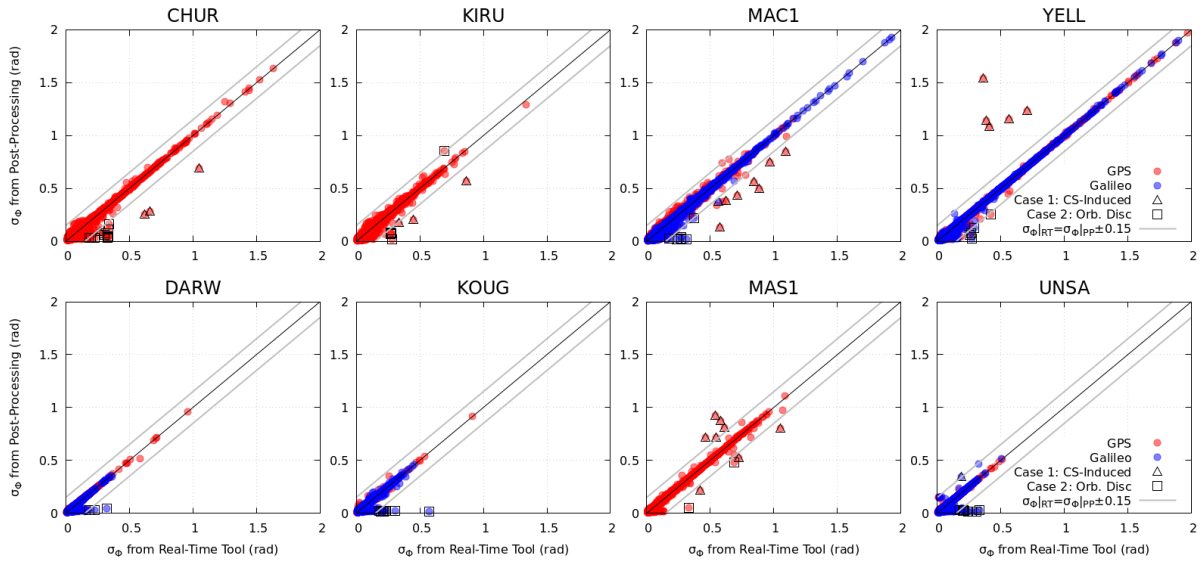

Fig. 3. Scatter plot of σ_ϕ, showing the correlation between σ_ϕ from RT tool (x-axis) and PP (y-axis), for high-latitude receivers CHUR, KIRU, MAC1, and YELL (top row) and low-latitude receivers DARW, KOUG, MAS1, and UNSA (bottom row). Results for the time period from DoY 104 to DoY 130 in 2023. Red and blue dots differentiate GPS and Galileo measurements, respectively. The black line represents the case where the two values are numerically equal, and gray lines delimit outliers with a difference in the value of σ_ϕ greater than 0.15 rad. Two typical outlier cases are marked: triangle (Case 1: CS-induced difference) and square (Case 2: orbit discontinuity).

TABLE I
SUMMARY OF RECEIVERS AND OUTLIERS IN THE RT VERSUS PP GD COMPARISON

Station	Lon (°)	Lat (°)	Dip (°)	Case 1: CS-induced	Case 2: Orb. Disc	Total sample
CHUR	-94.09	58.59	80.36	4	12	186921
KIRU	20.97	67.72	77.46	3	5	183054
MAC1	158.94	-54.32	-79.06	8	6	331955
YELL	-114.48	62.32	80.76	5	5	337835
DARW	131.13	-12.76	-40.16	0	3	345180
KOUG	-52.64	5.06	16.29	0	9	282686
MAS1	-15.63	27.61	36.45	8	2	196587
UNSA	-65.41	-24.58	-24.58	1	10	308297

Fig. 3 shows the scatter plots of the σ_ϕ index from the RT tool (horizontal axis) versus the corresponding values from PP (vertical axis) obtained in common 60-s intervals. GPS and Galileo measurements are marked with red and blue dots, respectively. The processed data covered from DoY 104 to DoY 130 in 2023 for the eight stations. However, during some time periods of DoY 128, anomalies were observed in the satellite clock RT products. Therefore, measurements from those periods were excluded to avoid impairing the validation. Finally, to mitigate the impact of multipath noise and model errors, an elevation cutoff angle of 30° was applied in the comparison.

The top panels of Fig. 3 (high-latitude stations) show generally higher σ_ϕ values compared to the bottom panels (low-latitude stations). In any case, it can be observed that the results show a great coherence between RT and PP values at all stations for the two constellations, particularly for high σ_ϕ values. It should be noted that, in the absence of scintillation, the calculation of the σ_ϕ index will be dominated by the thermal noise of the device plus the noise coming from the modeling of the geodetic corrections. Consequently, one can see in Fig. 3 that the cloud of points is wider for the lowest values of the phase scintillation index, narrowing as the values of σ_ϕ increase.

Despite this consistency, some outliers can be observed, particularly when setting a threshold of 0.15 rad (gray lines in Fig. 3) for the difference on σ_ϕ values. Upon investigation, two typical cases for these outliers were identified.

1) CS-Induced Difference (Triangles in Fig. 3): These outliers can be attributed to two primary factors. First, observations from RT streams occasionally experience data gaps, whereas PP RINEX files typically maintain continuous data. These gaps in RT streams can shorten the arc available for computation, affecting directly the derived index. Second, differences in the detection of a CS between the RT and PP tools. The PP tool, unconstrained by RT requirements, eliminates observations during the transition time of a CS, retaining only measurements from consolidated arcs. In contrast, the RT processing lacks this step, leading to minor differences in their observations when a CS occurs. In less frequent cases, CSs close to the detection threshold can introduce discrepancies of the detection solutions between RT and PP tools, despite the detection threshold being the same in both cases. This discrepancy results in different σ_ϕ values in the two processing.

2) Orbit Discontinuity (Squares in Fig. 3): Discontinuities sometimes occur in satellite orbits following the updates of the ultrarapid orbit products used in RT. These discontinuities, which mostly affect Galileo satellites since there are fewer ground stations collecting Galileo data for orbit estimation, cause artificial jumps in the detrended carrier-phase residuals. Although far less frequently, this can also be observed in GPS orbits. However, the postprocessed orbits from IGS used

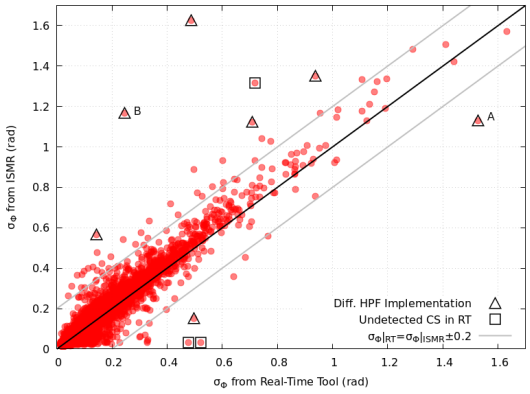

Fig. 4. Scatter plot of σ_ϕ from CHUR using the RT tool (x-axis) and the ISMR values from CHUC (y-axis) during the validation period. The black solid line indicates equal values. The largest outliers marked with triangles, and squares and labels are commented in the text.

by the PP GD have removed these anomalies. Consequently, discrepancies of up to 0.3 rad are observed in the comparison of σ_ϕ producing the small tails seen in the lower left of the plots in Fig. 3 for all stations tracking the Galileo satellites.

Fig. 3 shows that 95% of the outliers can be attributed to the two aforementioned cases. Table I (columns 5–7) provides a breakdown of number of these outlier cases across all stations, along with the total number of samples. The remaining outliers, which cannot be clearly attributed to these cases, represent a negligible fraction of the data. Overall, the outlier percentage is only 0.004% of the total number of samples from all receivers, indicating a minor impact on the performance of the RT tool.

IV. Validation With ISMR

The Septentrio PolaRxS ISMR named CHUC, belonging to the CHAIN network [7] (http://chain.physics.unb.ca/chain/), has a baseline of about 100 m with respect to the geodetic TPS NET-G3A receiver CHUR from the RT GONet. Both receivers are in the magnetic polar cap region, at 58.6°N, 94.1°W, with magnetic dip 80.4°. This has allowed for an additional validation study of the RT σ_ϕ index using the ISMR output values as a reference result. The ISMR CHUC computes the standard 60-s σ_ϕ from carrier phase measurements at 50 Hz. This same index is calculated in the RT tool using observations at 1 Hz.

Fig. 4 shows the scatter plot of the σ_ϕ index, obtained from the RT solution for the geodetic receiver CHUR (horizontal axis) versus the corresponding output from the ISMR (vertical axis), for the same time period used in the validation analysis of Section III and for the same set of 60-s intervals in the two devices. Neither device provides Galileo measurements, so only GPS satellites with elevations above 30° were considered. A total of 177 212 comparisons were performed.

Note that observations after a CS in the RT processing for CHUR are excluded from the 60-s interval in the calculation of σ_ϕ. In contrast, the ISMR CHUC does not apply any CS checking to its high-frequency measurements, using all data from the 60-s time interval to derive the corresponding σ_ϕ index. The impact on the σ_ϕ values of undetected CSs in the ISMR data has been reported in previous studies [12]. Therefore, in order to have a fair comparison in Fig. 4, the 60-s intervals in which a CS was detected in the geodetic receiver CHUR were eliminated.

One can observe in Fig. 4 that the results closely align with the diagonal black line corresponding to equal values. Despite being two receivers from different manufacturers, with different clocks and a moderate baseline, the comparison shows acceptable agreement, even for the values of σ_ϕ greater than 1 rad. The cases giving an absolute value of the σ_ϕ difference greater than 0.2 rad correspond to points outside the gray lines in Fig. 4. A small tendency toward larger σ_ϕ values from the ISMR data is appreciated. This is reasonable, as the geodetic receiver CHUR at 1 Hz cannot sample ionospheric fluctuations lasting less than 1 s, unlike the ISMR CHUC, which uses measurements every 0.02 s.

However, this difference in the sampling frequency of the measurements used by each receiver is not the cause of the largest outliers observed in Fig. 4 (squares and triangles). These outliers are due to differences between the high-pass filter (HPF) used by the Septentrio PolaRxS ISMR software and the RT tool. The Butterworth HPF used by the ISMR to derive the σ_ϕ index is based on a classic forward implementation. Thus, the filtered signal at a given 60-s time interval will be affected by past values in previous time intervals. Instead, the Butterworth HPF implementation in the RT tool is based on a forward–backward strategy, without using measurements outside the 60-s data batch, to achieve a zero-phase filtering [18], avoiding the phase shift impact on the filtered signal.

After analyzing the raw carrier phases from the ISMR CHUC (at 50 Hz) and its RINEX files (at 1 Hz), we have confirmed that all the cases marked with a triangle in Fig. 4 show a fast fluctuation in the detrended carrier phase a few seconds around the boundary of the 60-s interval, in which the discrepancy between the σ_ϕ values occurred. However, upon examining the ionospheric fluctuations from the L1 detrended carrier phase, we found that the two receivers, geodetic and ISMR, track the same time evolution of the fluctuations. There is no inherent reason for the big difference in the σ_ϕ values. One example is presented in Fig. 5 for two cases corresponding to consecutive time intervals, the triangles labeled A and B in Fig. 4.

An ultimate verification that the origin of those outliers is the difference in the HPF implementation was obtained by applying the same forward Butterworth HPF used by the ISMR to the RT detrended carrier phases, which then renders a similar value of σ_ϕ as the one reported originally by the ISMR. In particular, for the cases A and B in Figs. 4 and 5, the values derived from the RT processing were 1.53 and 0.25 rad, respectively, but using the classic forward implementation of the HPF, the new values obtained were 1.13 and 1.17 rad, respectively, which are equal to the values issued by the ISMR.

On the other hand, the outliers marked with a square in Fig. 4 have a different origin. They are produced by undetected CSs in the RT processing of the geodetic TPS receiver CHUR, which produce a discontinuity in the detrended L1 carrier phase. However, the Septentrio ISMR does not show a CS

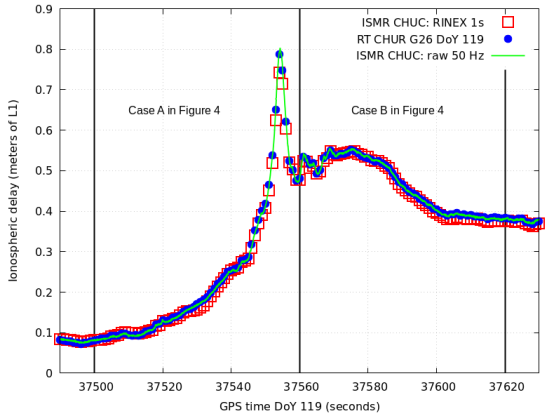

Fig. 5. Ionospheric delay in the detrended L1 carrier phase from satellite G26 for outliers labeled A and B in Fig. 4. Vertical lines delimit time intervals of 60 s. ISMR CHUC from 1-to 50-Hz data (squares and green line, respectively). Geodetic receiver CHUR from RT 1-Hz data (blue dots).

in the same time period. This produces a different shape of the detrended carrier phase between the two receivers. The undetected CSs in CHUR correspond to small discontinuities in the boundary of the threshold used by the RT tool for CS detection [12]. The detection of this type of CSs is a challenge that deserves further study. Nevertheless, their impact on the present comparison is very minor as can be seen in Fig. 4.

V. Conclusion

The present contribution aimed to extend the GD technique from PP to RT for the monitoring of ionospheric scintillation based on worldwide networks of geodetic receivers. To this end, we have developed a tool that uses RT carrier phase measurements and RT satellite orbit, clock, and tropospheric corrections, implementing an RT estimate of the receiver clock offsets and CS detection. Comparing the results with the PP GD, we conclude that the RT implementation achieves results highly consistent with the demonstrated PP tool. Furthermore, for a geodetic receiver nearby an ISMR, the comparison also shows satisfactory consistency. In both comparisons, the higher outliers have been analyzed, and the causes of the large differences have been identified. Consequently, we conclude that the RT implementation of the GD shows adequate reliability to monitor and characterize scintillation by means of the σ_ϕ index at a worldwide scale.

References

[1] P. M. Kintner, B. M. Ledvina, and E. R. de Paula, "GPS and ionospheric scintillations," *Space Weather*, vol. 5, no. 9, pp. 1–23, Sep. 2007, doi: 10.1029/2006sw000260.

[2] A. W. Wernik, J. A. Secan, and E. J. Fremouw, "Ionospheric irregularities and scintillation," *Adv. Space Res.*, vol. 31, no. 4, pp. 971–981, Jan. 2003, doi: 10.1016/s0273-1177(02)00795-0.

[3] G. de Oliveira Nascimento Brassarote, E. M. de Souza, and J. F. G. Monico, "S 4 index: Does it only measure ionospheric scintillation?" *GPS Solutions*, vol. 22, no. 1, pp. 1–12, Nov. 2017, doi: 10.1007/s10291-017-0666-x.

[4] B. Breitsch, Y. T. Morton, C. Rino, and D. Xu, "GNSS carrier phase cycle slips due to diffractive ionosphere scintillation: Simulation and characterization," *IEEE Trans. Aerosp. Electron. Syst.*, vol. 56, no. 5, pp. 3632–3644, Oct. 2020, doi: 10.1109/TAES.2020.2979025.

[5] A. J. V. Dierendonck, J. A. Klobuchar, and Q. Hua, "Ionospheric scintillation monitoring using commercial single frequency C/A code receivers," in *Proc. 6th Int. Tech. Meeting Satell. Division Inst. Navigat. (ION GPS)*, Salt Lake City, UT, USA, Sep. 1993, pp. 1333–1342.

[6] B. C. Vani, M. H. Shimabukuro, and J. F. G. Monico, "Visual exploration and analysis of ionospheric scintillation monitoring data: The ISMR query tool," *Comput. Geosci.*, vol. 104, pp. 125–134, Jul. 2017, doi: 10.1016/j.cageo.2016.08.022.

[7] P. T. Jayachandran et al., "Canadian high Arctic ionospheric network (CHAIN)," *Radio Sci.*, vol. 44, no. 1, pp. 1–10, Feb. 2009, doi: 10.1029/2008RS004046.

[8] K. Guo, Y. Zhao, Y. Liu, J. Wang, C. Zhang, and Y. Zhu, "Study of ionospheric scintillation characteristics in Australia with GNSS during 2011–2015," *Adv. Space Res.*, vol. 59, no. 12, pp. 2909–2922, Jun. 2017, doi: 10.1016/j.asr.2017.03.007.

[9] V. Romano et al., "The electronic space weather upper atmosphere (eSWua) project at INGV: Advancements and state of the art," *Annales Geophysicae*, vol. 26, no. 2, pp. 345–351, Feb. 26, 2008, doi: 10.5194/angeo-26-345-2008.

[10] J. M. Juan, A. Aragon-Angel, J. Sanz, G. González-Casado, and A. Rovira-Garcia, "A method for scintillation characterization using geodetic receivers operating at 1 Hz," *J. Geodesy*, vol. 91, no. 11, pp. 1383–1397, Nov. 2017, doi: 10.1007/s00190-017-1031-0.

[11] J. M. Juan et al., "Feasibility of precise navigation in high and low latitude regions under scintillation conditions," *J. Space Weather Space Climate*, vol. 8, pp. 1–11, Sep. 2018, doi: 10.1051/swsc/2017047.

[12] V. K. Nguyen et al., "Measuring phase scintillation at different frequencies with conventional GNSS receivers operating at 1 hz," *J. Geodesy*, vol. 93, no. 10, pp. 1985–2001, Oct. 2019, doi: 10.1007/s00190-019-01297-z.

[13] A. Rovira-Garcia, G. González-Casado, J. M. Juan, J. Sanz, and R. O. Pérez, "Climatology of high and low latitude scintillation in the last solar cycle by means of the geodetic detrending technique," in *Proc. Int. Tech. Meeting Inst. Navigat.*, Feb. 13, 2020, pp. 920–933, doi: 10.33012/2020.17187.

[14] G. Weber and L. Mervart, "The BKG ntrip client (BNC)," in *Proc. Report EUREF Symp.*, 2007, pp. 1–12.

[15] A. Rovira-Garcia, J. M. Juan, J. Sanz, G. González-Casado, and E. Bertran, "Fast precise point positioning: A system to provide corrections for single and multi-frequency navigation," *Navigation*, vol. 63, no. 3, pp. 231–247, Sep. 2016, doi: 10.1002/navi.148.

[16] C. C. Timote et al., "Ionospheric corrections tailored to Galileo HAS: Validation with single-epoch navigation," *GPS Solutions*, vol. 28, no. 2, p. 93, Mar. 26, 2024, doi: 10.1007/s10291-024-01630-w.

[17] J. S. Subirana, J. M. J. Zornoza, and M. Hernández-Pajares, *GNSS Data Processing. Volume I:, Fundamentals and Algorithms*. Noordwijk, Netherlands: ESA Communications, 2013, pp. 95–138.

[18] F. Gustafsson, "Determining the initial states in forward–backward filtering," *IEEE Trans. Signal Process.*, vol. 44, no. 4, pp. 988–992, Apr. 1996, doi: 10.1109/78.492552.